Nanoscale

PAPER

View Article Online
View Journal

Cite this: DOI: 10.1039/d2nr02056d

Room temperature giant magnetoresistance in half-metallic Cr_2C based two-dimensional tunnel junctions†

Shreeja Das, Arnab Kabiraj and Santanu Mahapatra *

Two-dimensional (2D) magnetic materials inherit enormous potential to revolutionize next-generation spintronic technology. The majority of prior investigations using 2D ferromagnet-based tunnel junctions have shown encouraging tunnel magnetoresistance (TMR) at low temperatures. Using first-principles-based calculations, here we investigate the magnetic properties of commercially available Cr_2C crystals at their monolayer limit and reveal their half metallicity properties far beyond room temperature. We then design hetero-multilayer structures combining Cr_2C with graphene and hexagonal boron nitride (h-BN) and report their magnetoresistance using spin-polarized quantum transport calculations. While graphene based devices, adsorbed on the metal contact, reveal a very high TMR (1200%), it can be further increased to 1500% by changing the barrier layer to h-BN. The dependence of TMR on the number of barrier layers and different metallic electrode materials (Ti, Ag, and Au) are also studied. Our investigation suggests that Cr_2C based spin valves can serve as the perfect building blocks for room temperature all-2D spintronic devices.

Received 14th April 2022,
Accepted 27th May 2022

DOI: 10.1039/d2nr02056d

rsc.li/nanoscale

Introduction

The discovery of magnetism in 2D materials is a fairly new and unexplored avenue. Even though the Mermin–Wagner postulate[1] limits the presence of a long-range magnetic order in two dimensions, monolayers of CrI_3, $Cr_2Ge_2Te_6$, VSe_2, Fe_3GeTe_2, *etc.* have been shown to be magnetic at finite temperatures due to the presence of magnetic anisotropy.[2] Thus, 2D magnets provide a rich arena for understanding magnetic order and manipulating spin at ultra-low dimensions for applications in spintronics,[3–6] memory storage devices,[7,8] magneto-optical devices,[9] neuromorphic computing,[10] and quantum computing devices. A magnetic tunnel junction (MTJ) is the fundamental building block of spintronic technology. In the literature, 2D ferromagnets have been used to design two types of MTJs: spin filter MTJs and spin-valve MTJs. Spin filter MTJs simply consist of a magnetic 2D material (*e.g.*, CrI_3, $CrPS_4$, WSe_2, VSe_2, $CoBr_2$, $FeCl_2$, *etc.*) sandwiched between conducting materials (Cu, Au, graphene, 1T-MoS_2, 1T-VSe_2, *etc.*).[11–19] On the other hand, spin valve MTJs are designed by sandwiching a (nonmagnetic) spacer tunneling layer (*e.g.*, h-BN, MoS_2, graphene, and InSe) in between conducting ferromagnetic layers (*e.g.*, Fe_3GeTe_2 and 1T-$CrTe_2$).[20–25]

The important criteria for selecting conducting ferromagnetic layers in all-2D vertical spin-valve MTJs are that they should possess a large perpendicular magnetic anisotropy, be thermodynamically stable at the monolayer limit, and have a high Curie temperature (*i.e.*, preferably maintaining ferromagnetism at room temperature). Apart from a very few,[26] most of the previous studies report MTJs involving 2D materials with low Curie temperature, and thus their room temperature application is questionable. A recent systematic high-throughput study has revealed the presence of out-of-plane anisotropy and high Curie temperature for Cr_2C,[27] which is the highest among all 2D ferromagnets with a perpendicular easy magnetization axis. Cr_2C belongs to the class of 2D MXenes, which can generally be chemically exfoliated from the parent bulk MAX (M = metal, X = carbon/nitrogen and A = aluminum) phase. From a practical fabrication point of view, most magnetic MXenes like Ta_3C_2, Ti_3C_2, and Ti_3N_2 lose their magnetism on surface passivation with O, H, and F functional groups.[28] However, Cr_2C is known to be an exception and retains its magnetic moments even in the presence of surface passivation.[29] Cr_2C is also available with a commercial vendor (**https://www.2dsemiconductors.com**) for experimental studies. Due to its half-metallic nature, Cr_2C provides high spin polarization, which can be useful for more efficient spin injection in magnetic tunnel junction (MTJ) devices. It has been shown to induce spin polarization and bandgap opening in adjacent graphene

Nano-Scale Device Research Laboratory, Department of Electronic Systems Engineering, Indian Institute of Science (IISc), Bangalore, Bangalore 560012, India. E-mail: santanu@iisc.ac.in

† Electronic supplementary information (ESI) available. See DOI: **https://doi.org/10.1039/d2nr02056d**

monolayers.[30] The large half-metallic gap can also be effective in preventing spin–flip scattering across the device during transport. Moreover, half-metals are also known to have low Gilbert damping,[31] which is suitable for low power consuming storage devices.[32] Vertical all-2D spin valves have earlier been fabricated using layers of Fe_3GeTe_2 (FGT) ferromagnet with up to 6 layers of semiconducting MoS_2 spacer layers in between and found to have eight times higher magnetoresistance than bulk MTJs, albeit at a very low temperature of 10 K.[21] High tunnel magnetoresistance (TMR) and spin injection values can be obtained only when the current in the parallel configuration is much higher than the anti-parallel configuration for either of the two spins. This makes half-metallic materials ideal for designing high TMR MTJs since they allow the transmission of only one type of spin-polarized current.

In the present study, we first demonstrate the stability of ferromagnetic Cr_2C at room temperature using first principles density functional theory (DFT) calculations, and Monte-Carlo and molecular dynamics simulations. We then design vertical spin-valve MTJs using different 2D barrier materials such as graphene and hexagonal boron nitride (h-BN) and investigate the spin injection and tunneling magnetoresistance (TMR) in such devices using spin-polarized quantum transport studies. Our studies show very high tunnel magnetoresistance values of up to 1500% at a finite voltage bias applied to the electrodes.

Results

Monolayer Cr_2C – electronic structure and stability

A Cr_2C monolayer consists of a layer of carbon atoms sandwiched between two layers of Cr atoms, as shown in Fig. 1(a). Previously, Cr_2C has been predicted to be a half-metallic ferromagnet using DFT-HSE06 calculations.[33] Fig. 1(a) shows the crystal structure of monolayer Cr_2C and Fig. 1(b) shows the spin-polarized electronic band structure of monolayer Cr_2C obtained from DFT calculations with a Hubbard correction of U = 5 eV. The optimized lattice constant was found to be a = 3.2018 Å, with each Cr atom possessing a magnetic moment of about $4\mu_B$. This is in good agreement with previous theoretical investigations on Cr_2C.[30,33] Using GGA-PBE functionals to calculate the electronic band structure, a spin gap of 1.6 eV is observed for the minority spin states, whereas the majority spin states show metallic nature. The metallic nature of the spin-up bands is mostly due to the Cr-3d orbitals with some contributions from C-2p orbitals, as seen in the projected density of states and band structure in ESI Fig. S1.† We also performed DFT calculations using different levels of Hubbard corrections (U = 3, 4, and 6 eV) to verify the intrinsic half-metallic nature of the material. Our calculations using DFT GGA + U with different values of U also confirm the half-metallic nature. The results are provided in Fig. S2 of the ESI.† In order to evaluate the thermodynamic stability of monolayer Cr_2C, the phonon dispersion spectrum was calculated using density functional perturbation theory (Fig. 1(c)). No negative frequency components were found in the phonon band structure indicating its dynamic stability.

Fig. 1(d) shows the variation in the magnetic moment for each Cr atom in the monolayer Cr_2C at 300 K as obtained from *ab initio* molecular dynamics (AIMD) simulations. The magnetic moment is maintained at around $4\mu_B$, indicating the structural stability of the monolayer at room temperature. For practical application in spintronics devices, the ferromagnet should retain its magnetism at room temperature. The easy axis of magnetization is oriented along the out-of-plane z-direction with a magnetic anisotropy value of 60.88 μeV per Cr atom. We performed classical Monte Carlo simulations based on the anisotropic Heisenberg Hamiltonian as described in the Methods section. The change in magnetization and susceptibility with temperature is shown in Fig. 1(e). As can be seen, monolayer Cr_2C is predicted to have a very high Curie temperature of 1152 K. The predicted values are much higher than most other 2D ferromagnets with perpendicular anisotropy making Cr_2C an ideal candidate material for designing 2D MTJs.

Cr_2C on metallic contacts

To design a true 2D MTJ, a monolayer of Cr_2C has to be adsorbed over suitable metallic contacts such as Au, Ti, Ag, Cu, Ir, Ru, *etc.* Here, we select the Au (111), Ag (111), and Ti (0001) surfaces, which were interfaced with a monolayer of Cr_2C with initial strains of 0.33%, 1.16%, and 1.70%, as shown in ESI Fig. S3.† DFT calculations reveal that the high magnetic moments on Cr in Cr_2C are well-preserved for the metal contact surfaces of Au (111) and Ag (111), with a change in the magnetic moment of about $0.11\mu_B$ and $0.07\mu_B$, respectively, whereas the Ti (0001) surface brings about a significant decrease ($0.19\mu_B$) in the magnetic moment of the monolayer Cr_2C. Therefore, we selected Au as the metallic contact for designing our MTJ device due to its lowest interfacial strain and lesser interference with the magnetic properties of Cr_2C.

Spin transport in Cr_2C based MTJ devices

2D MTJs were designed using a monolayer of Cr_2C adsorbed on bulk Au as the left and right electrodes, as shown in Fig. 2. Two types of barrier materials (graphene and h-BN) between the two ferromagnetic Cr_2C layers are considered in this study. 2D materials like h-BN, when used as the tunneling barrier between ferromagnetic layers, have been shown to significantly enhance spin injection in MTJs compared to bulk barrier materials.[34,35] The left and right electrodes were 7.29 Å in length. The central scattering region is 42.29 Å in length with sufficient screening length between the Au/Cr_2C interface and the Au electrodes to ensure a smooth variation of charge and potential in the region and avoid spurious scattering at the electrode interfaces. The current–voltage (I–V) characteristics at zero and finite bias voltages were investigated using the Landauer–Büttiker formula implemented in the non-equilibrium Green's function (NEGF) method,

$$I(V_{\text{bias}}) = \frac{e}{h}\int T(E, V_{\text{bias}})[f_L(E-\mu_L) - f_R(E-\mu_R)]\mathrm{d}E \qquad (1)$$

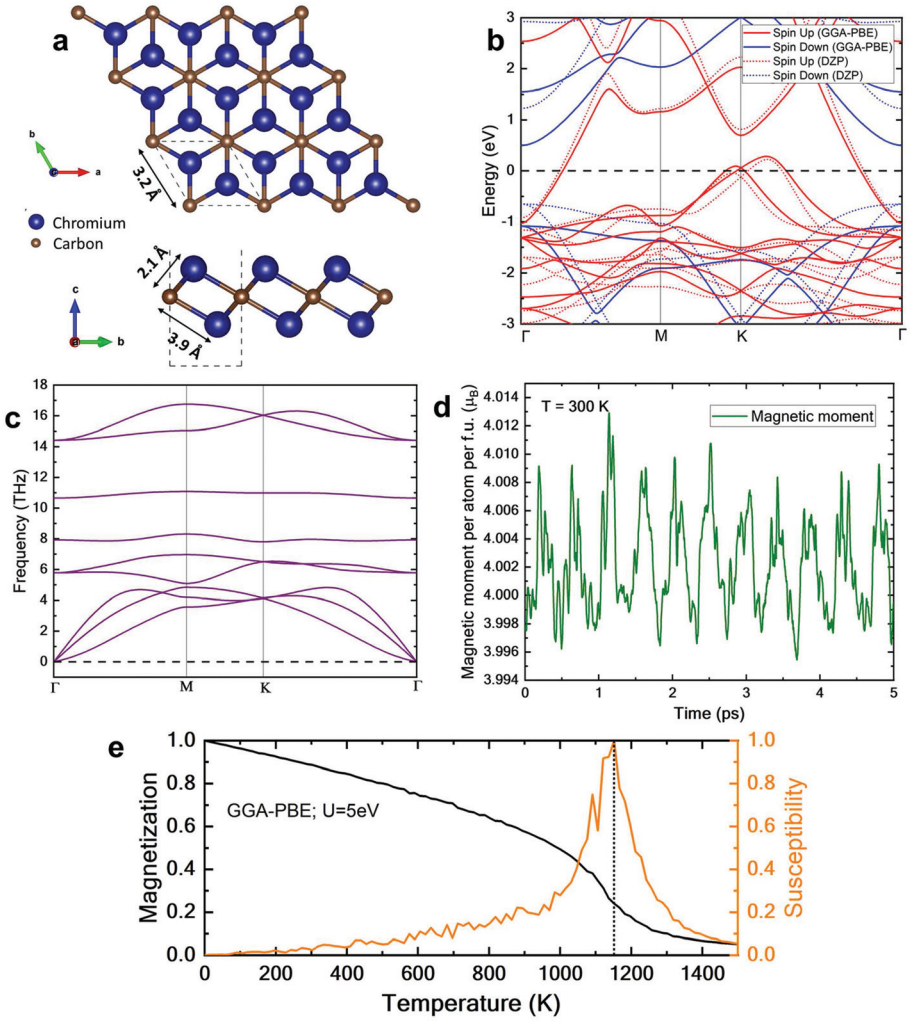

Fig. 1 (a) Crystal structure and (b) spin-resolved electronic band structure for exchange correlation functionals: GGA-PBE in VASP and pseudopotentials with double-zeta polarized (DZP) basis sets in QuantumATK, (c) phonon band structure, (d) magnetic moment of Cr_2C at 300 K from AIMD simulations, and (e) magnetization curves showing Curie temperatures using the GGA-PBE functional with U = 5 eV.

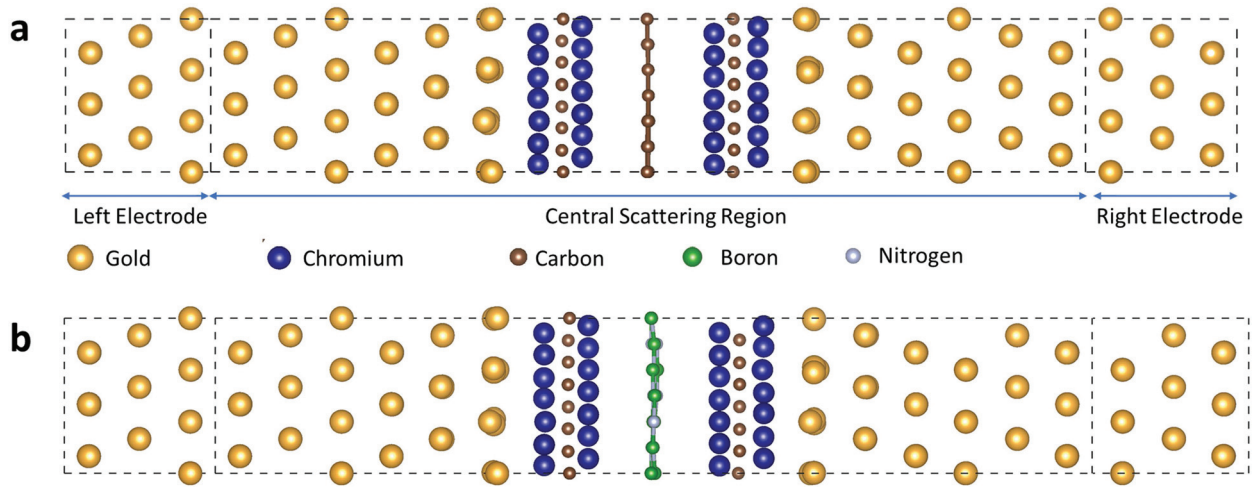

Fig. 2 Relaxed structures of the MTJ devices consisting of monolayer Cr_2C adsorbed on the Au (111) surface with (a) graphene and (b) h-BN spacer layers in between. The left/right electrodes and central scattering region are marked.

where $f_{L(R)}$ is the Fermi–Dirac distribution function of the left (right) electrode, and $T(E, V_{bias})$ is the transmission probability of spin-polarized carriers through the central scattering region at a particular energy, E, and applied voltage bias to the electrodes, V_{bias}. The TMR ratio can be found from the conductance (G) using the formula:

$$\mathrm{TMR} = \frac{G_P - G_{AP}}{G_{AP}} \times 100\% \quad (2)$$

where conductance, $G(E) = \frac{e^2}{h} T(E)$ (Siemens) and G_p, and G_{AP} are the total conductances in parallel and anti-parallel configurations, respectively. In addition, the spin injection efficiency, SIE (η) for a configuration can be found from the spin-polarized current as

$$\eta = \left| \frac{I_\uparrow - I_\downarrow}{I_\uparrow + I_\downarrow} \right| \times 100\% \quad (3)$$

where $I_{\uparrow(\downarrow)}$ is the spin-up (down) current.

For the graphene-barrier MTJ, the TMR values at different on-site Hubbard correction levels of U = 4, 5, and 6 eV were calculated for zero bias to be 1116.92%, 1185.40%, and 1017.66%, respectively. It can be seen that the variation of U has an insignificant effect on TMR. Hence, all subsequent studies were performed using U = 5 eV. The layer dependence of TMR was also calculated and is plotted in Fig. S4 of the ESI.† Increasing the number of spacer layers adversely affects the TMR values, which indicates that the tunneling current decreases due to the increasing barrier width as it increases scattering inside the tunneling region. As discussed earlier, the Ti (0001) surface causes a significant reduction of magnetic moments of the adsorbed Cr_2C layers, which is also reflected in the fact that for the MTJs with Ti(0001)-Cr_2C and the monolayer graphene barrier, the TMR value is decreased to about 950%.

Finite bias voltages ranging from −0.1 to 0.1 V with steps of 0.01 V were applied across the left and right electrodes of the MTJs. The total current and conductance for graphene and h-BN MTJs in the parallel (P) and anti-parallel (AP) magnetization configurations were calculated as shown in Fig. 3(a)–(d). The total current is the sum of spin-up ($I_\uparrow$) and spin-down currents ($I_\downarrow$). The parallel currents (I_P) are an order of magnitude larger than the anti-parallel currents (I_{AP}) for both devices giving rise to high TMR values. I_P in both MTJs are almost identical, but I_{AP} for the h-BN MTJ is lower than that of the graphene MTJ. Due to the insulating nature of h-BN, the conductance in both the parallel and anti-parallel configurations is much lower than that for the graphene barrier giving rise to higher TMR values for the h-BN MTJ. This is also corroborated by the $k_\parallel$-resolved transmission spectrum for parallel and anti-parallel configurations, as discussed later. The TMR and SIE values of the monolayer graphene MTJ and h-BN MTJ device calculated at finite bias are plotted in Fig. 3(e) and (f). For the graphene MTJ, the TMR value increases with increasing bias voltage, whereas the TMR value is high and remains mostly constant across a wide range of bias voltages for the h-BN MTJ. According to eqn (2), the TMR value is obtained from the total conductance in the parallel and anti-parallel configurations. As shown in Fig. 3(a) and (b), the total conductance in the anti-parallel configuration G_{AP} is mostly constant for the h-BN device across a wide range of voltages. In contrast, the conductance in the anti-parallel configuration G_{AP} for the graphene MTJ decreases monotonically with increasing bias voltage. To further understand this difference between the G_{AP} of h-BN and graphene MTJs, we plot the transmission coefficients in the anti-parallel configuration at different bias voltages in Fig. S10 of the ESI†. The conductance of spin-up carriers decreases with increasing bias in both graphene and h-BN MTJs. Conversely, the conductance of spin-down carriers in h-BN MTJ is found to increase under higher bias voltages.

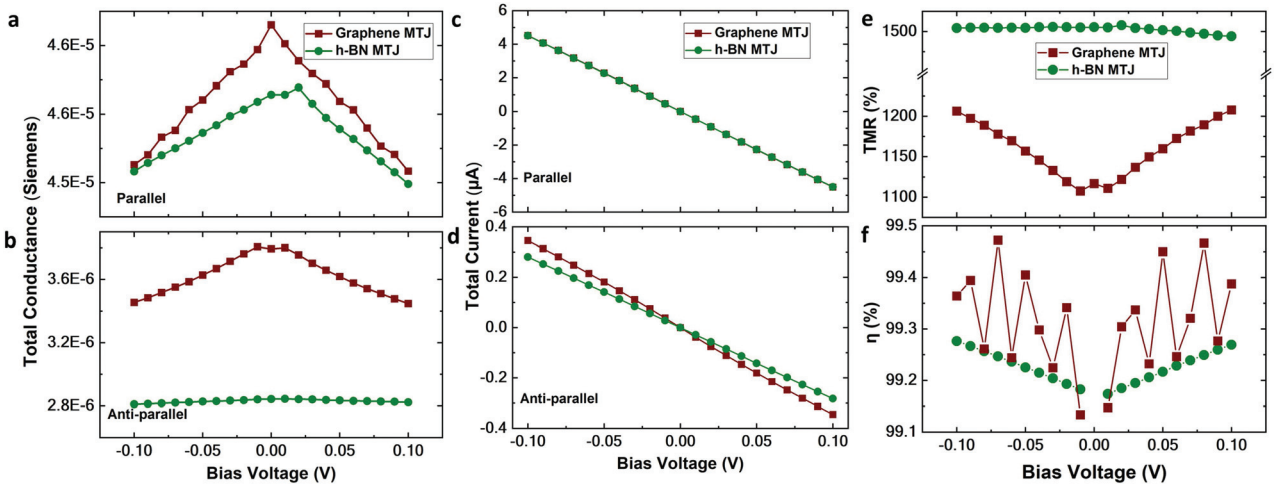

Fig. 3 Total conductance in the MTJs for (a) parallel and (b) anti-parallel magnetization configurations. Total current in the MTJs for (c) parallel and (d) anti-parallel magnetization configurations. (e) TMR and (f) SIE values of the graphene and h-BN MTJs under finite bias conditions. SIE is only reported for the parallel configuration.

Thus, the effect of decreased conductance of spin-up carriers is effectively cancelled by the increase in conductance of spin-down carriers, thereby rendering the total conductance to be more or less constant in the h-BN MTJ.

As shown in Fig. 3(f), the SIE for both devices follows markedly different trends with increasing bias voltage. From eqn (3), the SIE depends on how the device can restrict the transmission of the down-spin components of the current. In the case of perfect 100% spin filtering, none of the spin-down current is transmitted across the barrier in the MTJ. Additionally, from eqn (1), the current is obtained by integrating the transmission over the interval between the Fermi levels of the drain and source. Thus, in order to understand the behavior of SIE in the device, we compared the transmission coefficients of both spin-up and spin-down components of the current for the graphene- and h-BN-MTJs at finite biases in Fig. S7 of the ESI.† In Fig. S7 (a) and (b),† the transmission curves of the spin-up component in both devices follow similar trends, *i.e.*, it decreases with increasing bias voltages. However, for spin-down carriers, only the h-BN-MTJ shows a steady and uniform decrease in transmission (Fig. S7(d)†). There is no clear distinction between the curves for the transmission coefficients of spin-down carriers at different bias voltages for the graphene-MTJ (Fig. S7(c)†). As a result, where the SIE rises monotonically for the h-BN-MTJ under increasing bias it fluctuates for the graphene-MTJ, which is reflected in Fig. 3(f).

Fig. 4 shows the $k_{\parallel}$-resolved transmission coefficients projected onto the 2D-Brillouin zone at the Fermi level and zero bias voltage for the MTJs designed with a single layer of graphene and h-BN as barriers. In the parallel (P) state, the conductance in both MTJs is dominated by hotspots at the edges of the Brillouin zone, at points M and K for the spin-up channel, whereas the spin-down conductance is zero (Fig. 4(a) and (d), (c) and (f)). This is the origin of a nearly 100% spin filtering effect at the Fermi level for both MTJs. In the anti-parallel (AP) configuration, spin-up carriers in the graphene MTJ show some conductance only at the edge of the central region of the Brillouin zone (Fig. 4(b)). On the other hand, for the h-BN MTJ, the spin-up conductance is negligible in the AP configuration (Fig. 4(e)). As a result, the TMR values for h-BN MTJs are higher than those for graphene MTJs. Spin injection efficiencies for both devices are high and nearly 100%.

The spatial distribution of electrons can be discerned from the renormalized electron localization function (ELF).[45] Regions with a full electron localization are depicted with a value of 1, and regions with no electrons are assigned a value of 0. Fig. 5 shows the in-plane electron localization function on the graphene and h-BN barrier layers in the MTJs at zero bias. The behavior was found to be similar for both spin-up and spin-down charges on the barrier layers, *i.e.*, both spin-up and spin-down charges accumulate uniformly over C–C bonds in the graphene layer and preferentially over N atoms in the h-BN layer. This is due to the heteropolar nature of B–N bonds where N is more electronegative than B. Thus, there is no electron localization on the top of B atoms, and all electrons of both spins are concentrated on N atoms only. In addition to the in-plane ELF highlighting the difference between interatomic bonding on the graphene and h-BN barrier layers, we have mapped the ELF along the transmission direction of the device (out-of-plane) in Fig. S8 and S9 of the ESI.† For both MTJs in a parallel configuration, the electrons of both spins are localized equally on the two Cr_2C layers. However, for the MTJs in an anti-parallel configuration, the left and right Cr_2C layers behave differently. The intralayer bonding in the right Cr_2C layer favors the concentration of spin-up carriers,

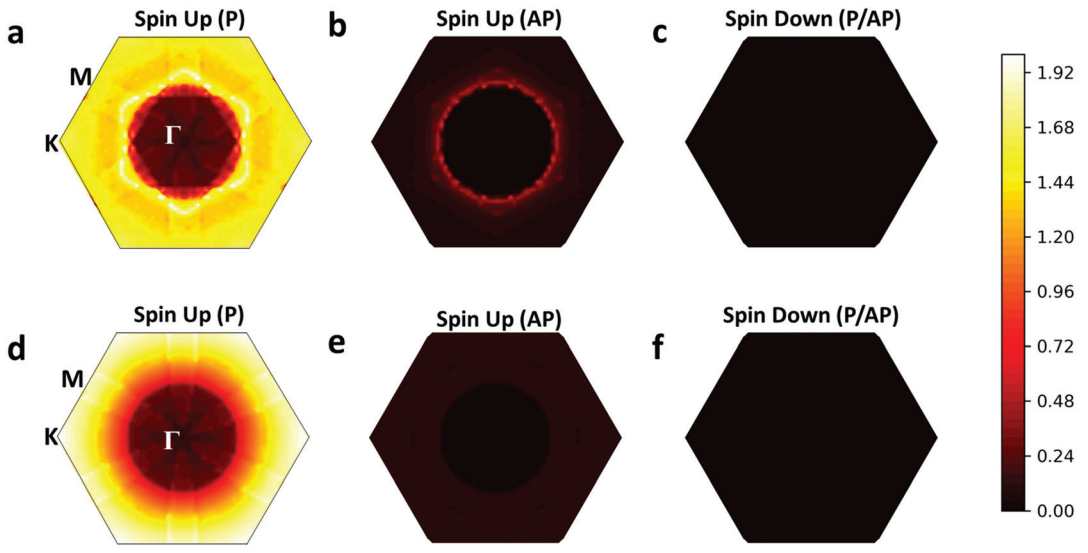

Fig. 4 : $k_{\parallel}$-Resolved transmission spectrum for the Cr_2C MTJ with (a)–(c) a monolayer graphene spacer and (d)–(f) a monolayer h-BN spacer at E = 0 eV and V_{bias} = 0 V. Panels from left to right indicate the spin-up transmission in a parallel magnetization configuration, spin-up transmission in an anti-parallel configuration, and spin-down transmission in both parallel and anti-parallel configurations, respectively.

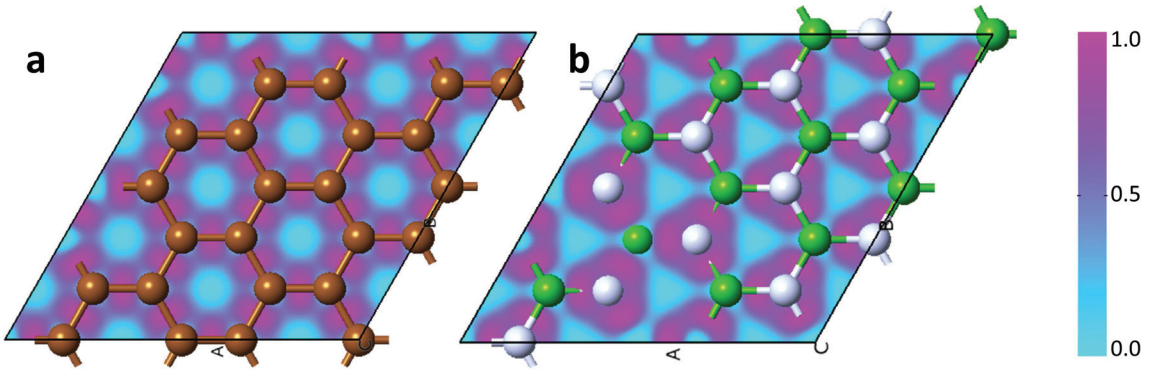

Fig. 5 Electron localization function on the (a) graphene and (b) h-BN spacer layers in the MTJ devices.

whereas the spin-down carriers are more localized on the left Cr_2C layer.

The spin-resolved projected local density of states of both the graphene and h-BN barrier MTJ devices in the real space at zero bias voltage along the transport direction is shown in Fig. 6 and 7. From Fig. 6(a) and (b), for the graphene MTJ in a parallel configuration, only spin-up states are transmitted across the device, and the spin-down states are completely blocked. For the anti-parallel configuration (Fig. 6(c) and (d)), spin-up states are missing in the right electrode, and spin-down states are missing in the left electrode. This causes a complete suppression of the transmission of each state in the anti-parallel configuration. This shows that the Cr_2C layers retain their half-metallic nature in the device and give rise to excellent spin filtering. Similar observations can be made for the h-BN MTJ in Fig. 7. Interestingly, on comparing the PLDOS of both devices in a parallel configuration, we notice that the barrier graphene layer remains conducting for both spin

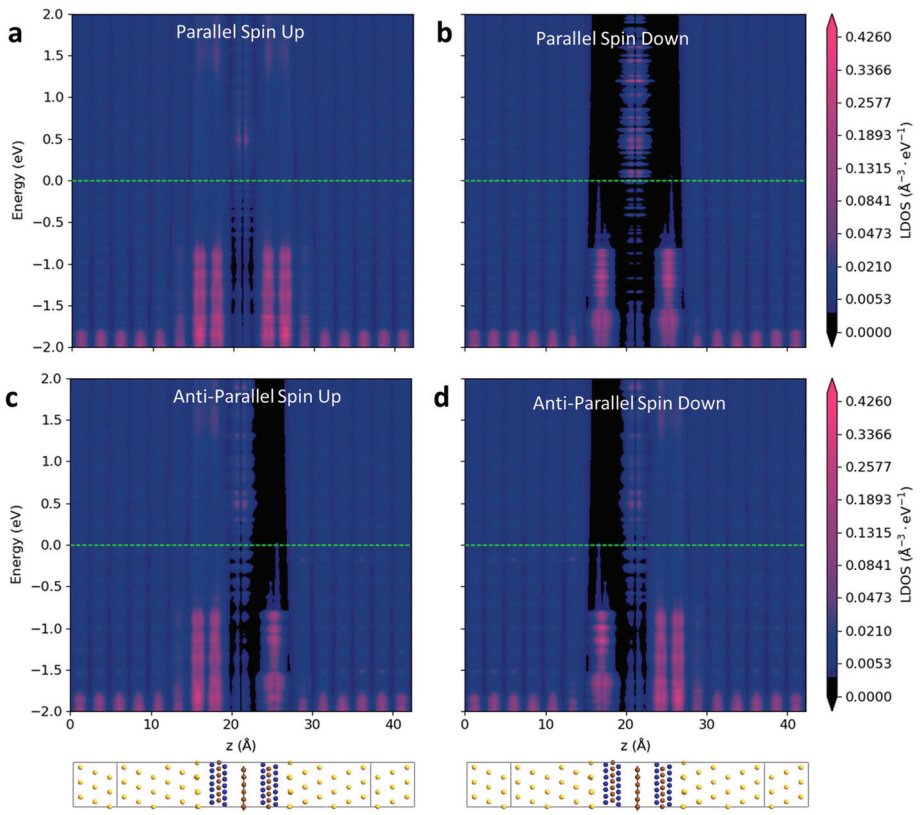

Fig. 6 Projected local density of states along the transport direction at equilibrium for the graphene MTJ. (a) Spin-up and (b) spin-down densities for the parallel configuration; (c) spin-up and (d) spin-down densities for the anti-parallel configuration. The Fermi level is denoted by the horizontal dashed line. Device structures in the *z*-direction are provided below the plot for reference.

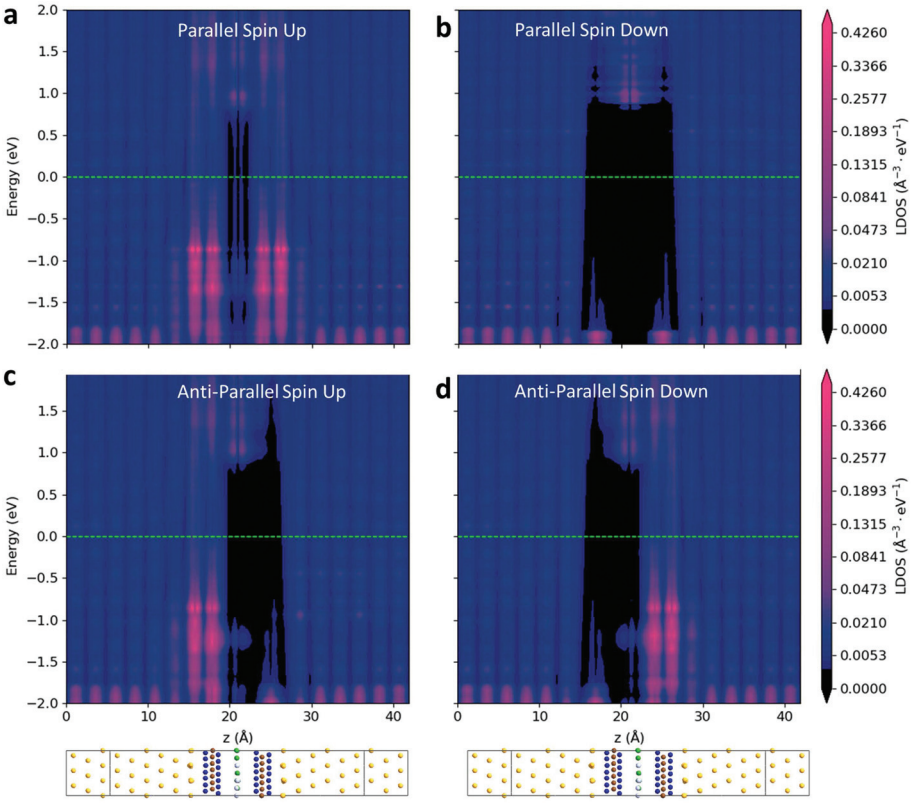

Fig. 7 Projected local density of states along the transport direction at equilibrium for the h-BN MTJ. (a) Spin-up and (b) spin-down densities for the parallel configuration; (c) spin-up and (d) spin-down densities for the anti-parallel configuration. The Fermi level is denoted by the horizontal dashed line. Device structures in the *z*-direction are provided below the plot for reference.

states, indicating lower spin injection at zero bias, which can be remedied by increasing the bias voltage as shown in Fig. 3(d). On the other hand, the h-BN layer (Fig. 6(c) and (d)) creates a thick barrier region of non-conductance for the spin-down states giving rise to higher TMR values and high spin injection in the h-BN barrier MTJ device.

Discussions

We investigated the unique half-metallic ferromagnetism properties of monolayer Cr_2C and its application in spintronics. The material is found to possess a very high Curie temperature (1152 K) as well as dynamic stability. Compared to other 2D materials, we noted that this is one of the highest reported Curie temperatures for a 2D ferromagnet, making it very suitable for spin manipulation operations at high temperatures. Moreover, it is also commercially available. Cr_2C was found to have a large perpendicular anisotropy, which is ideally suitable for vertical MTJ devices. From our results, we found Cr_2C to be well adsorbed over a bulk Au (111) surface with little lattice mismatch and small depletion in the magnetic moment of the Cr atoms. Thus, we suggest the design of a Cr_2C monolayer adsorbed over a bulk gold surface acting as the magnetic electrode of the MTJ. From our calculations, the vertical MTJ device designed with a Cr_2C ferromagnetic layer was found to have very high TMR values and almost 100% spin injection efficiency. Two different barrier layers were studied, graphene and h-BN, of which the h-BN barrier device has a higher TMR value of up to 1500% due to its insulating nature. The MTJ with graphene as a barrier was found to possess conducting states for both spin carriers near the Fermi level at the barrier layer in the parallel and anti-parallel configurations. Instead of graphene, we can use h-BN as a barrier layer, which completely blocks the transmission of carriers in the anti-parallel configuration leading to much higher TMR values. Another strategy to increase TMR is to apply a bias voltage across the electrodes. The TMR value of the graphene MTJ was found to increase up to 1200% on application of 100 mV bias. The effect of increasing the number of barrier layers was also studied, wherein the TMR value was found to decrease due to increased scattering in the barrier region. Our studies show that using the novel half-metallic MXene Cr_2C as a ferromagnetic electrode in vertical MTJs, we can achieve high spin injection for the spin-up carriers across the barrier layer and high TMR. Coupled with its extremely high Curie temperature, Cr_2C can emerge as an ideal material for fabricating ultra-thin, high density vertical all-2D MTJs, which can be operated at room temperature. Such devices can be compatible with existing high-temperature spintronic device (such as magnetic random access memory) fabrication processes.

Methods

Structural relaxations, electronic structure and magnetic moment calculations of all the devices were performed using the first principles Vienna *ab initio* Simulation Package (VASP) code,[36,37] which uses a plane wave basis set of wave functions. Projector augmented-wave (PAW) pseudopotentials[38,39] were used, and the exchange–correlation functional was described using the Perdew–Burke–Ernzerhof (PBE) functional within the generalized gradient approximation (GGA) scheme.[40] All structures were relaxed until the Hellman–Feynman force on each atom was less than 0.01 eV Å^{-1}. A kinetic energy cut-off of 520 eV was used with a Monkhorst *k*-point mesh of 3 × 3 × 1 density. The *k*-point mesh was taken as 21 × 21 × 1 for monolayer Cr_2C calculations. van der Waals corrections were applied using the DFT-D3 scheme.[46] Dipole–dipole interaction correction was also applied in the vertical direction (*i.e.*, out-of-plane, *z*-direction) to avoid errors due to the applied periodic boundary conditions. For all structures, a sizable vacuum of more than 10 Å was applied in the *z*-direction to avoid interaction with periodic images. On-site Coulomb corrections were implemented using the Hubbard parameter,[47] *U*, to account for the strong electronic correlations in the highly localized Cr-3d orbitals. The phonon dispersion spectrum was calculated using density functional perturbation theory in VASP and Phonopy.[41] Thermal stability calculations were performed using *ab initio* molecular dynamics (AIMD) calculations as implemented in VASP. The GGA-PBE functional with a Hubbard correction of 5 eV was used. A 4 × 4 supercell of monolayer Cr_2C was subject to a Nosé–Hoover thermostat under the canonical ensemble (NVT). The temperature was set at 300 K and a timestep of 2 fs was set. Spin-polarized simulations were allowed to run for a total of 5 ps.

To determine the Curie temperature, VASP-calculated collinear and noncollinear DFT energies are fitted to the following anisotropic Heisenberg spin Hamiltonian:

$$\begin{aligned} H = &-\frac{1}{2}J_1\sum_{i,j}\boldsymbol{S}_i\cdot\boldsymbol{S}_j-\frac{1}{2}J_2\sum_{i,k}\boldsymbol{S}_i\cdot\boldsymbol{S}_k-\frac{1}{2}J_3\sum_{i,l}\boldsymbol{S}_i\cdot\boldsymbol{S}_l\\ &-\frac{1}{2}K_{1x}\sum_{i,j}S_i^xS_j^x-\frac{1}{2}K_{1y}\sum_{i,j}S_i^yS_j^y-\frac{1}{2}K_{1z}\sum_{i,j}S_i^zS_j^z\\ &-\frac{1}{2}K_{2x}\sum_{i,k}S_i^xS_k^x-\frac{1}{2}K_{2y}\sum_{i,k}S_i^yS_k^y-\frac{1}{2}K_{2z}\sum_{i,k}S_i^zS_k^z\\ &-\frac{1}{2}K_{3x}\sum_{i,l}S_i^xS_l^x-\frac{1}{2}K_{3y}\sum_{i,l}S_i^yS_l^y-\frac{1}{2}K_{3z}\sum_{i,l}S_i^zS_l^z\\ &-A_x\sum_i(S_i^x)^2-A_y\sum_i(S_i^y)^2-A_z\sum_i(S_i^z)^2 \end{aligned} \quad (4)$$

where J_1, J_2, and J_3 terms represent isotropic exchange between the 1st, 2nd, and 3rd nearest magnetic neighbors, respectively. $\boldsymbol{S}_i$ is the spin of the site in question, and $\boldsymbol{S}_j$, $\boldsymbol{S}_k$, and $\boldsymbol{S}_l$ are the spins of sites at 1st, 2nd, and 3rd nearest magnetic neighbor shells, which are all 3D vectors. The individual spin components are represented as S_n^d, where $n = i, j, k$, and l and $d = x$, y, and z. The K_{md} terms represent the anisotropic exchange for neighbor shell m (m = 1, 2, and 3) and direction d ($d = x$, y, and z). The A_d terms represent the single-ion anisotropy for direction d. Note that the $\frac{1}{2}$ factor for the exchange terms is there to counter the effect of double counting. Because of the hexagonal cell of Cr_2C, it is difficult to obtain the anisotropy terms for both the x and y directions. We assume that the material is magnetically isotropic in the whole x–y plane, *i.e.*, we assume an XXZ model, which is usually a reasonable approximation for 2D magnets.[42,43] This results in $K_{mx} = K_{my}$ (m = 1, 2, and 3) and $A_x = A_y$. The different spin configurations whose energies are used to perform the fitting are shown visually in Fig. S5.† The corresponding energies, the fitted equations to solve, and their solutions are presented in detail in Table S1.† The Hubbard *U* correction term has been varied, but a minimal change was observed in the determined T_c. This is shown in Fig. S6.† To study the ferromagnetic (FM) to paramagnetic (PM) transition in the material, Monte Carlo (MC) simulations of the above-mentioned model have been performed using the Metropolis algorithm with the single-spin update scheme. To eliminate the size effects, a 50 × 50 supercell with in-plane periodic boundary conditions containing 2500 sites has been used to simulate the system. In total, 10^5 Monte Carlo steps have been performed for each temperature, while the results from the first 10^4 steps have been discarded, as the system is allowed to equilibrate (thermalize) during this time. The final values of magnetization and susceptibility are calculated as the average over the last 9 × 10^4 MC steps for each temperature.

The electronic and spin transport calculations were performed with the non-equilibrium Green's function (NEGF) method using the QuantumATK (v2021.06-SP1)[44] tool. The PBE functional is used within the spin-polarized GGA scheme. Transport calculations were performed using pseudopotentials with double-zeta polarized (DZP) basis sets for all the atomic species with the on-site Hubbard correction of U = 5 eV for the Cr atoms. Self-consistent calculations were performed using a density mesh cut-off of 155 Hartree and a gamma-centered *k*-point mesh of 21 × 21 × 300. A denser *k*-mesh of 64 × 64 was used to sample the 2D Brillouin zone for the transmission calculations and *I*–*V* characteristics.

Author contributions

S. D. designed the MTJ, conducted the transport calculations, and analysed the final results. A. K. conducted the Monte-Carlo simulations. S. M. conceived the problem statement and overall supervised the work. All authors contributed to the manuscript writing.

Conflicts of interest

There are no conflicts to declare.

Acknowledgements

This work was supported by the Core Research Grant (CRG) scheme of the Science and Engineering Research Board (SERB), Government of India, under Grant No. CRG/2020/000758. The authors thank Supercomputer Education and Research Centre (SERC), Indian Institute of Science (IISc) Bangalore, for facilitating the Roddam Narasimha Cluster and PARAM-Pravega supercomputer.

References

1 N. D. Mermin and H. Wagner, *Phys. Rev. Lett.*, 1966, **17**, 1133–1136.
2 C. Gong and X. Zhang, *Science*, 2019, **363**, eaav4450.
3 E. C. Ahn, *npj 2D Mater. Appl.*, 2020, **4**, 17.
4 X. Lin, W. Yang, K. L. Wang and W. Zhao, *Nat. Electron.*, 2019, **2**, 274–283.
5 G. Hu and B. Xiang, *Nanoscale Res. Lett.*, 2020, **15**, 226.
6 J. F. Sierra, J. Fabian, R. K. Kawakami, S. Roche and S. O. Valenzuela, *Nat. Nanotechnol.*, 2021, **16**, 856–868.
7 S. Bertolazzi, P. Bondavalli, S. Roche, T. San, S.-Y. Choi, L. Colombo, F. Bonaccorso and P. Samorì, *Adv. Mater.*, 2019, **31**, 1806663.
8 C. Chappert, A. Fert and F. N. Van Dau, *Nat. Mater.*, 2007, **6**, 813–823.
9 Y. Fang, S. Wu, Z.-Z. Zhu and G.-Y. Guo, *Phys. Rev. B*, 2018, **98**, 125416.
10 J. Grollier, D. Querlioz, K. Y. Camsari, K. Everschor-Sitte, S. Fukami and M. D. Stiles, *Nat. Electron.*, 2020, **3**, 360–370.
11 T. Song, X. Cai, M. W.-Y. Tu, X. Zhang, B. Huang, N. P. Wilson, K. L. Seyler, L. Zhu, T. Taniguchi, K. Watanabe, M. A. McGuire, D. H. Cobden, D. Xiao, W. Yao and X. Xu, *Science*, 2018, **360**, 1214–1218.
12 H. H. Kim, B. Yang, T. Patel, F. Sfigakis, C. Li, S. Tian, H. Lei and A. W. Tsen, *Nano Lett.*, 2018, **18**, 4885–4890.
13 K. Dolui, M. D. Petrović, K. Zollner, P. Plecháč, J. Fabian and B. K. Nikolić, *Nano Lett.*, 2020, **20**, 2288–2295.
14 T. R. Paudel and E. Y. Tsymbal, *ACS Appl. Mater. Interfaces*, 2019, **11**, 15781–15787.
15 J. Yang, S. Fang, Y. Peng, S. Liu, B. Wu, R. Quhe, S. Ding, C. Yang, J. Ma, B. Shi, L. Xu, X. Sun, G. Tian, C. Wang, J. Shi, J. Lu and J. Yang, *Phys. Rev. Appl.*, 2021, **16**, 024011.
16 Y. Feng, X. Wu, L. Hu and G. Gao, *J. Mater. Chem. C*, 2020, **8**, 14353–14359.
17 H. Liu, P. Wang, L. Pan, H. Wen, Y. Liu, H. Wu, Y. Zong, X. Jiang, Z. Wei and J. Xia, *J. Magn. Magn. Mater.*, 2021, **539**, 168346.
18 Y. Zhu, X. Y. Guo, L. N. Jiang, Z. R. Yan, Y. Yan and X. F. Han, *Phys. Rev. B*, 2021, **103**, 134437.
19 F. Li, B. Yang, Y. Zhu, X. Han and Y. Yan, *Appl. Surf. Sci.*, 2020, **505**, 144648.
20 Z. Wang, D. Sapkota, T. Taniguchi, K. Watanabe, D. Mandrus and A. F. Morpurgo, *Nano Lett.*, 2018, **18**, 4303–4308.
21 H. Lin, F. Yan, C. Hu, Q. Lv, W. Zhu, Z. Wang, Z. Wei, K. Chang and K. Wang, *ACS Appl. Mater. Interfaces*, 2020, **12**, 43921–43926.
22 S. Albarakati, C. Tan, Z.-J. Chen, J. G. Partridge, G. Zheng, L. Farrar, E. L. H. Mayes, M. R. Field, C. Lee, Y. Wang, Y. Xiong, M. Tian, F. Xiang, A. R. Hamilton, O. A. Tretiakov, D. Culcer, Y.-J. Zhao and L. Wang, *Sci. Adv.*, 2019, **5**, eaaw0409.
23 H. Zhou, Y. Zhang and W. Zhao, *ACS Appl. Mater. Interfaces*, 2021, **13**, 1214–1221.
24 L. Zhang, T. Li, J. Li, Y. Jiang, J. Yuan and H. Li, *J. Phys. Chem. C*, 2020, **124**, 27429–27435.
25 X. Li, J.-T. Lü, J. Zhang, L. You, Y. Su and E. Y. Tsymbal, *Nano Lett.*, 2019, **19**, 5133–5139.
26 Q. Wu and L. K. Ang, *Appl. Phys. Lett.*, 2022, **120**, 022401.
27 A. Kabiraj, M. Kumar and S. Mahapatra, *npj Comput. Mater.*, 2020, **6**, 35.
28 M. N. Abdelmalak, PhD thesis, Drexel University, 2014.
29 M. Khazaei, M. Arai, T. Sasaki, C.-Y. Chung, N. S. Venkataramanan, M. Estili, Y. Sakka and Y. Kawazoe, *Adv. Funct. Mater.*, 2013, **23**, 2185–2192.
30 B. Zhou, S. Ji, Z. Tian, W. Cheng, X. Wang and W. Mi, *Carbon*, 2018, **132**, 25–31.
31 C. Liu, C. K. A. Mewes, M. Chshiev, T. Mewes and W. H. Butler, *Appl. Phys. Lett.*, 2009, **95**, 022509.
32 R. K. Ghosh, A. Jose and G. Kumari, *Phys. Rev. B*, 2021, **103**, 054409.
33 C. Si, J. Zhou and Z. Sun, *ACS Appl. Mater. Interfaces*, 2015, **7**, 17510–17515.
34 M. V. Kamalakar, A. Dankert, J. Bergsten, T. Ive and S. P. Dash, *Sci. Rep.*, 2015, **4**, 6146.
35 T. Yamaguchi, Y. Inoue, S. Masubuchi, S. Morikawa, M. Onuki, K. Watanabe, T. Taniguchi, R. Moriya and T. Machida, *Appl. Phys. Express*, 2013, **6**, 073001.
36 G. Kresse and J. Hafner, *Phys. Rev. B: Condens. Matter Mater. Phys.*, 1994, **49**, 14251.
37 G. Kresse and J. Hafner, *Phys. Rev. B: Condens. Matter Mater. Phys.*, 1993, **48**, 13115–13118.
38 P. E. Blöchl, *Phys. Rev. B: Condens. Matter Mater. Phys.*, 1994, **50**, 17953–17979.
39 G. Kresse and D. Joubert, *Phys. Rev. B: Condens. Matter Mater. Phys.*, 1999, **59**, 1758.
40 J. P. Perdew, K. Burke and M. Ernzerhof, *Phys. Rev. Lett.*, 1996, **77**, 3865.
41 A. Togo and I. Tanaka, *Scr. Mater.*, 2015, **108**, 1–5.
42 D. Torelli and T. Olsen, *2D Mater.*, 2018, **6**, 015028.
43 D. Torelli, K. S. Thygesen and T. Olsen, *2D Mater.*, 2019, **6**, 045018.
44 S. Smidstrup, T. Markussen, P. Vancraeyveld, J. Wellendorff, J. Schneider, T. Gunst, B. Verstichel, D. Stradi, P. A. Khomyakov, U. G. Vej-Hansen, M.-E. Lee, S. T. Chill, F. Rasmussen, G. Penazzi, F. Corsetti,

A. Ojanperä, K. Jensen, M. L. N. Palsgaard, U. Martinez, A. Blom, M. Brandbyge and K. Stokbro, *J. Phys.: Condens. Matter*, 2020, **32**, 015901.

45 A. Savin, R. Nesper, W. Steffen and T. M. Fassler, *Angew. Chem., Int. Ed. Engl.*, 1997, **36**(17), 1808–1832.

46 S. Grimme, J. Antony, S. Ehrlich and H. Krieg, *J. Chem. Phys.*, 2010, **132**(15), 154104.

47 S. L. Dudarev, G. A. Botton, S. Y. Savrasov, C. J. Humphreys and A. P. Sutton, *Phys. Rev. B*, 1998, **57**(3), 1505.